

# Inverse design of promising electrocatalysts for CO<sub>2</sub> reduction via generative models and bird swarm algorithm

Received: 10 May 2024

Accepted: 17 December 2024

Published online: 26 January 2025

Zhilong Song<sup>1,3</sup>, Linfeng Fan<sup>1,2,3</sup>, Shuaihua Lu<sup>1</sup>, Chongyi Ling<sup>1</sup>,  
Qionghua Zhou<sup>1,2</sup>✉ & Jinlan Wang<sup>1,2</sup>✉

Directly generating material structures with optimal properties is a long-standing goal in material design. Traditional generative models often struggle to efficiently explore the global chemical space, limiting their utility to localized space. Here, we present a framework named Material Generation with Efficient Global Chemical Space Search (MAGECS) that addresses this challenge by integrating the bird swarm algorithm and supervised graph neural networks, enabling effective navigation of generative models in the immense chemical space towards materials with target properties. Applied to the design of alloy electrocatalysts for CO<sub>2</sub> reduction (CO<sub>2</sub>RR), MAGECS generates over 250,000 structures, achieving a 2.5-fold increase in high-activity structures (35%) compared to random generation. Five predicted alloys—CuAl, AlPd, Sn<sub>2</sub>Pd<sub>5</sub>, Sn<sub>9</sub>Pd<sub>7</sub>, and CuAlSe<sub>2</sub> are synthesized and characterized, with two showing around 90% Faraday efficiency for CO<sub>2</sub>RR. This work highlights the potential of MAGECS to revolutionize functional material development, paving the way for fully automated, artificial intelligence-driven material design.

Machine learning (ML), owing to its ability to analyze vast datasets and identify complex correlations, has revolutionized the material science landscape<sup>1–4</sup>. Currently, a widely-used ML approach, known as forward design, involves utilizing ML algorithms to establish structure-property relationships and predicts properties of unknown materials through element substitution within existing materials<sup>5–9</sup>. However, it is extremely challenging to identify novel and useful candidates in chemical spaces that are overwhelming in size, *e.g.*, the chemical space of inorganic compounds, which contains approximately 10<sup>N</sup> possible configurations for compounds with N atoms in the unit cell<sup>10</sup>. Furthermore, a fundamental drawback of the forward design is that it cannot generate materials beyond structural prototypes of existing materials. In recent years, generative models, particularly those based on deep learning architectures, have emerged as powerful tools to overcome the drawbacks of forward design for discovering materials (Figure S1)<sup>11,12</sup>. These models leverage large datasets of material properties and structures to learn complex patterns and correlations. By

capturing the intricate interplay between various material attributes, generative models can generate new materials that meet specific criteria. This strategy is named inverse design<sup>11</sup>. This transformative capability not only accelerates the discovery process but also expands the scope of materials exploration beyond what was previously conceivable<sup>13</sup>.

Two popular generative models, the variational autoencoder (VAE) and the generative adversarial network (GAN) have been successfully applied to inversely design stable V-O<sup>14</sup>, Bi-Se<sup>15</sup>, Mg-Mn-O<sup>16</sup> material systems, zeolites with desired methane heat of adsorption<sup>17</sup>, stable cubic semiconductors<sup>18,19</sup> and MOFs for carbon dioxide separation<sup>20</sup>. However, these generative models are often limited to the generation of structures with a given symmetry or composition. Most recently, the crystal diffusion variational autoencoder (CDVAE) based on graph neural networks (GNN) has been developed to generate diverse crystal structures with acceptable quality<sup>21</sup>, *i.e.*, structures that have reasonable compositions (overall charge neutrality), proper

<sup>1</sup>Key Laboratory of Quantum Materials and Devices of Ministry of Education, School of Physics, Southeast University, Nanjing 21189, China. <sup>2</sup>Suzhou Laboratory, Suzhou 215125, China. <sup>3</sup>These authors contributed equally: Zhilong Song, Linfeng Fan. ✉e-mail: [qh.zhou@seu.edu.cn](mailto:qh.zhou@seu.edu.cn); [jlwang@seu.edu.cn](mailto:jlwang@seu.edu.cn)

bond lengths, and thermodynamic stability. Nevertheless, generative models inherently learn patterns from large and diverse training datasets to achieve the generation of high-quality structures. Consequently, they tend to generate material structures that closely resemble the training dataset, where material structures with superior properties are usually rare. This suggests we need additional algorithms to guide the generative model to escape away from the restriction of the training data and simultaneously maintain the generation quality. Meanwhile, the immensity of the material property space presents significant challenges for global and efficient exploration. On the other hand, the current inverse design methods used for designing materials with targeted properties lack universality, necessitating the training of different generative models for different properties<sup>14–20</sup>. This methodology fails to leverage a plethora of accurate property prediction models already available, which use various material descriptors, both compositional and structural<sup>6,7,9,22–25</sup>. As a result, the capability of inverse design is restricted to a narrow set of properties, primarily formation energy.

In this work, we address the aforementioned challenges by developing a general inverse design framework, Material Generation with Efficient global Chemical space Search (MAGECS), which integrates bird swarm algorithm (BSA)<sup>26,27</sup>, crystal diffusion variational autoencoder (CDVAE) and supervised graph neural network (GNN). The introduction of BSA can efficiently steer the generator towards generating structures with target property via optimizing latent space vectors, which serve as the input for generative models to construct structures, in the property space. This transforms the generation of structures from the traditional random generation to purposeful and efficient exploration of property space based on targeted properties. Using MAGECS, we realize the first generative model-based inverse design of novel alloy electrocatalysts for CO<sub>2</sub> reduction reaction (CO<sub>2</sub>RR)—a pivotal step in mitigating greenhouse gas emissions and promoting the carbon cycle<sup>28–31</sup>. To effectively evaluate the CO<sub>2</sub>RR activity of alloys, we utilize the optimal adsorption energy of CO ( $\Delta E_{\text{CO}}$ ), which is usually the key intermediate in electrocatalytic CO<sub>2</sub>RR<sup>8,32</sup>. Out of the 250,000 alloy surfaces we generated, the

proportion of structures with high CO<sub>2</sub>RR activity is 2.5 times higher than structures randomly generated by CDVAE. Next, among these highly active alloy surfaces, we further consider the competitive hydrogen evolution reaction (HER) and thermodynamic stability, and screen the top 110 potential surfaces for further verification with first-principles calculations. To the end, we successfully synthesized five innovative alloy catalysts, CuAl, AlPd, Sn<sub>2</sub>Pd<sub>5</sub>, Sn<sub>6</sub>Pd<sub>7</sub>, and CuAlSe<sub>2</sub>, and two of which exhibit high CO<sub>2</sub>RR activity ( $\sim 600.6 \text{ mA cm}^{-2}$  and  $\sim 296.2 \text{ mA cm}^{-2}$  current density under  $-1.1 \text{ V}$  vs. RHE) and selectivity (around 90% CO<sub>2</sub>RR Faraday efficiency).

## Results

### Inverse design framework of MAGECS

Our inverse design framework MAGECS comprises two primary domains of operation: the generation of new surfaces in structure space and the global optimization of generated surfaces in property space (Fig. 1). First, we employ the CDVAE pretrained generative model to create new surfaces with both high quality and diversity. The CDVAE model is trained on a database containing various catalyst surfaces created by Tran *et al.* (GASpy) (Table S1) and generates new structures (*i.e.*, surfaces in this work) from latent vectors (steps I–II in Fig. 1). Specifically, these latent vectors are fed into three fully connected neural networks which respectively output the atomic number, lattice constant, and composition/stoichiometry (Figure S2). A surface can be built using these outputs and randomly generated atom coordinates. Then, the surface stoichiometry and coordinates were adjusted to be reasonable by the Langevin dynamics in CDVAE.

Second, to realize the optimization of generated surfaces in property space, we need to rapidly assess the CO<sub>2</sub> activity of these generated surfaces. Here the adsorption energy of the key intermediate CO ( $\Delta E_{\text{CO}}$ ) is selected as the learning target. To this end, we enumerate all possible adsorption sites on the surface and add CO on these sites (step III in Fig. 1). We trained a supervised graph neural network (DimeNet ++), recognized for its invariance to crystal structures and high accuracy in predicting material properties<sup>33,34</sup>, to predict the  $\Delta E_{\text{CO}}$  of all sites. To ensure the applicability of predicting the

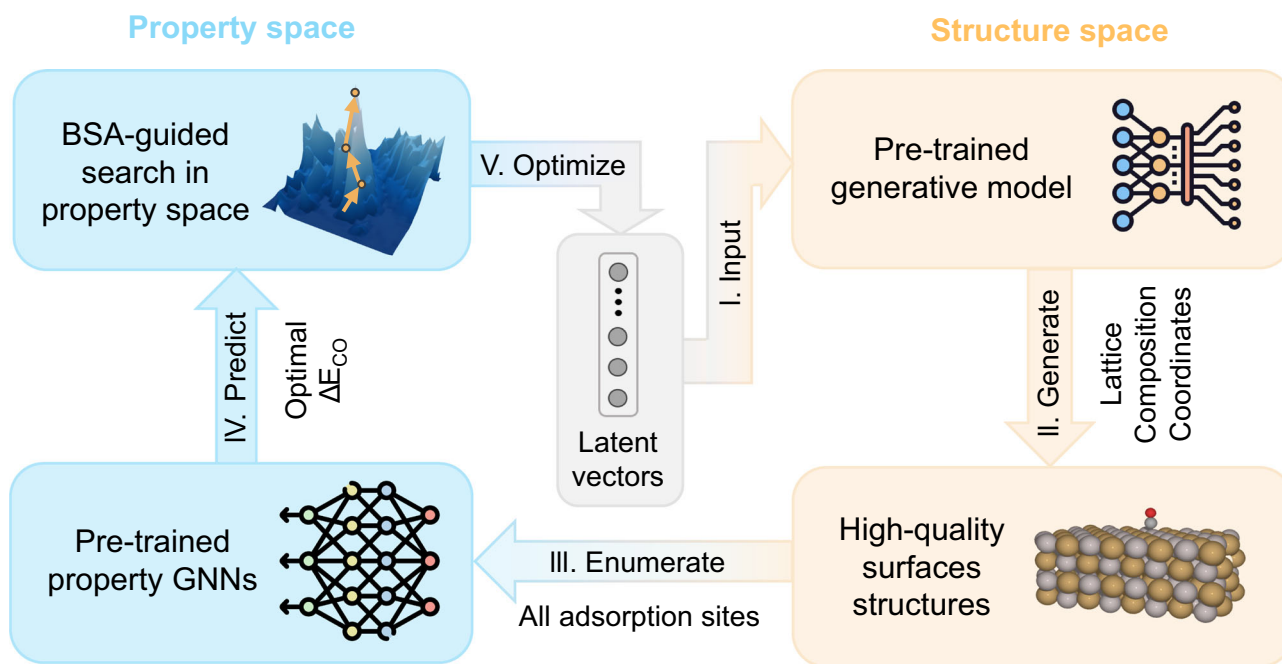


**Fig. 1 | Schematic diagram of inverse design materials with desired properties using our framework (surfaces for CO<sub>2</sub>RR in this work).** It contains three main parts: surface structures generation from latent vectors via generative model (step

I–II), CO adsorption energy prediction via supervised GNN model (step III–IV) and optimization of CO<sub>2</sub>RR properties via BSA (step V).

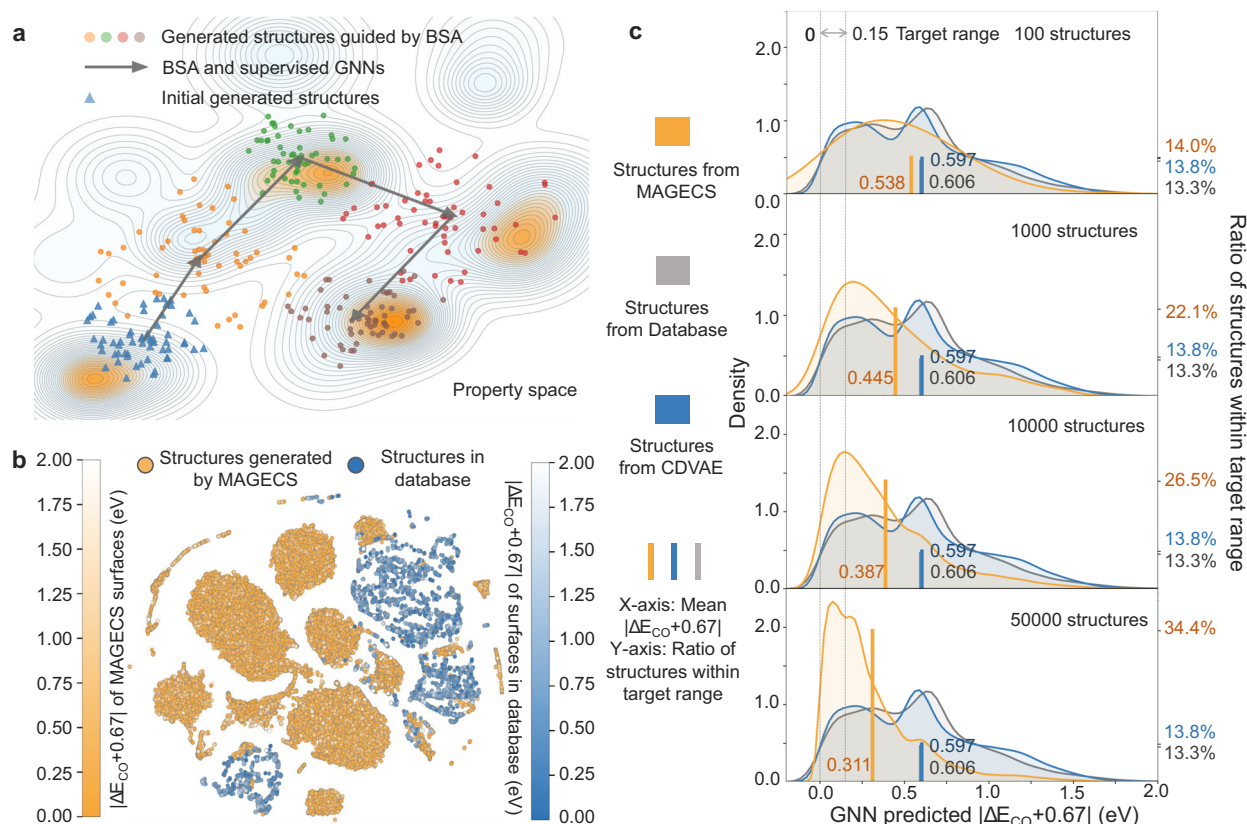


**Fig. 2 | Advantages of MAGECS.** **a** Structures generated by CDVAE (colored dots) are optimized by BSA and supervised models (arrows), facilitating the global and efficient exploration of the property space. The contour lines represent the topography of the property space, where the peaks correspond to materials with desirable properties (e.g., high performance), and the valleys indicate regions of lower property values. The density of the contour lines reflects the gradient of the property landscape, with closer lines indicating steeper changes in properties. **b** T-SNE visualization of the structures in dataset (blue points) and MAGECS

generated structures (orange points) using our framework. The darker the color of the point, the better the  $\text{CO}_2\text{RR}$  activity. **c** Comparison of the distribution of  $|\Delta E_{CO} + 0.67|$ , the average value of  $|\Delta E_{CO} + 0.67|$  (X-axis of columns) and the proportion of structures satisfying  $|\Delta E_{CO} + 0.67| \leq 0.15$  eV (Y-axis of columns) among MAGECS, CDVAE generated structures and training set structures. From top to bottom, the four figures illustrate the comparison where MAGECS generated 100, 1000, 10,000, and 50,000 structures, respectively.

$\Delta E_{CO}$  of generated surfaces, the DimeNet++ model was trained using exactly the same surface structures used to train the generation model. Next, the minimal predicted adsorption energies of all sites are used as fitness for evaluating latent vectors (step IV in Fig. 1). It is noteworthy that our framework is compatible with any form of property prediction model, regardless of the type of material descriptors they utilize, whether based on composition or structure. This enables our framework to optimize any material properties without altering the generative model.

Third, to steer the generator toward generating active surfaces for  $\text{CO}_2\text{RR}$  (i.e., to globally optimize the latent vectors in the property space), we integrate the BSA algorithm which was inspired by the swarm intelligence observed in bird swarms. As depicted in Figure S2, birds in nature exhibit three main social behaviors: foraging, vigilance, and flight. By modeling these interactions, BSA not only exhibits superior optimization efficiency but also has a high capability of escaping from local optimum. In this work, BSA first generates a batch of birds (i.e., latent vectors in Figure S3), which can be used to generate an equal number of surface structures. The activity of these surfaces is evaluated by DimeNet++ and then fed back to BSA to generate new latent vectors (step V in Fig. 1). This process will be iterated until a number of predetermined generations are reached.

To sum up, the BSA and supervised models are employed to guide (arrows in Fig. 2a) the optimization of the CDVAE-generated structures in the property space, enabling rapid discovery of new structures beyond the training database (blue points in Fig. 2a) with good

properties (peaks in Fig. 2a). Figure 2b visualizes the T-SNE plot of generated and training surface structures using latent space vectors (features) obtained by the encoder in CDVAE, revealing that our framework indeed explores a much larger chemical space with potentially high  $\text{CO}_2\text{RR}$  activity than that covered by the training database. Notably, this training database, deriving from active learning methods and automated DFT calculations, already covers a vast chemical space. This further proves the superiority of our inverse design framework in globally and efficiently exploring the chemical space.

### Results of inverse design framework and evaluation of generated surfaces

To realize the global optimization of generated surfaces for  $\text{CO}_2\text{RR}$  in the property space, the optimization target is first required to be set. The optimal  $\Delta E_{CO}$  value for  $\text{CO}_2\text{RR}$  is  $-0.67$  eV, which was used in a pioneering study on active learning for  $\text{CO}_2\text{RR}$  alloys<sup>8</sup>. This value was identified by microkinetic modeling, which  $\Delta E_{CO}$  exhibits a volcano plot relationship with the experimental  $\text{CO}_2$  reduction rate and selectivity, with the peak of the volcano corresponding to  $\Delta E_{CO}$  at  $-0.67$  eV<sup>32</sup>. Considering the mean absolute error (MAE) of the DimeNet++ model (0.143 eV on testing data), we set the criterion with  $|\Delta E_{CO} + 0.67| \leq 0.15$  eV to be favorable and used it as the optimization target for BSA.

MAGECS was then executed three times, each comprising 500 BSA steps (100 structures each step). In all three runs, the BSA can lead the generative model to go beyond the training data (Figure S4),



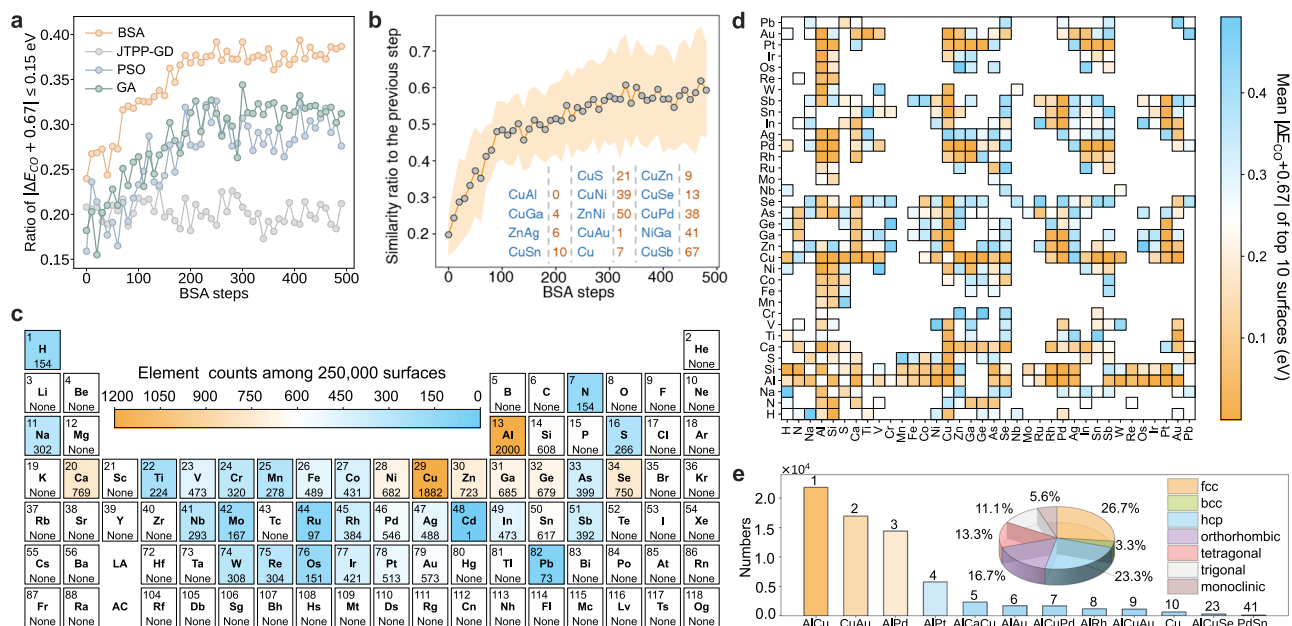


**Fig. 3 | Results of inverse design alloy surfaces for CO<sub>2</sub>RR. a** Average proportion of surfaces with  $|\Delta E_{\text{CO}} + 0.67| \leq 0.15$  eV measured at every ten steps of the optimization process using bird swarm algorithm (BSA) (orange), jointly trained property predictor combined with gradient descent (JTPP-GD) (grey), particle swarm optimization (PSO) (green) and genetic algorithm (GA) (blue). **b** Mean surface similarity ratio in every ten steps during BSA optimization of four runs. Inset shows the number of steps rediscovering formerly reported surfaces with high CO<sub>2</sub>RR performance. **c** Preferences of elements across 250,000 generated surfaces,

with increasing orange intensity indicating the greater quantity of element.

**d** Predicted activity distribution for generated bimetallic alloy surfaces. The more orange the color, the lower the average of the lowest ten  $|\Delta E_{\text{CO}} + 0.67|$  of surfaces. **e** Top composition of 250,000 generated surfaces with  $|\Delta E_{\text{CO}} + 0.67| \leq 0.15$  eV. The more orange the color, the more frequently this composition appears. The number on the bar represents the rank, the subfigure shows the crystal system distribution of the bulk structure of these surfaces.

demonstrating the effectiveness of MAGECS. Note that there is no further improvement in the number of generated surfaces meeting  $|\Delta E_{\text{CO}} + 0.67| \leq 0.15$  eV after 200–300 BSA steps. In order to validate this finding and generate more promising surface structures with high CO<sub>2</sub>RR activity, one additional run with 1000 BSA steps was conducted. Hence, a total of 250,000 alloy surfaces were generated.

To reveal the advantage of MAGECS, we employed the conventional CDVAE model to produce 50000 new surfaces and compare the distribution of predicted  $|\Delta E_{\text{CO}} + 0.67|$  across surfaces generated by MAGECS, CDVAE, and those within the training set. As shown in Fig. 2c, the CDVAE successfully reproduced the distribution of  $|\Delta E_{\text{CO}} + 0.67|$  of training surfaces, with both the average  $|\Delta E_{\text{CO}} + 0.67|$  and proportion of surfaces satisfying  $|\Delta E_{\text{CO}} + 0.67| \leq 0.15$  eV (highly active surfaces) closely aligning. In contrast, among the 100, 1000, 10,000 and 50,000 structures iteratively generated by MAGECS, the proportion of highly active surfaces was rapidly improved, ultimately being 2.5 times higher than those generated by CDVAE and from training data. The above merits showcase the efficacy of our BSA to steer the generative model to mass-generate structures with properties beyond training data.

Building upon this, we conducted a thorough analysis of BSA optimization process using the average performance of four runs (Figure S4–S6 detail the results of each run) and the mean value of every ten BSA steps considering the deviation during optimization. The proportion of surfaces with  $|\Delta E_{\text{CO}} + 0.67| \leq 0.15$  eV out of 100 generated surfaces in each step increases rapidly as BSA runs, eventually maintaining around 38% after 200 steps, which yields a considerable number of desired surfaces (Fig. 3a). Meanwhile, 78.9% of the generated surfaces exceed the training and validation sets, proving the powerful capability of MAGECS to create new materials with enhanced properties. To further demonstrate the efficiency of MAGECS, we compared the BSA-guided property optimization with three other optimization approaches, each generating 50,000 surfaces: (I) jointly trained property predictor combined with gradient descent (JTPP-GD),

(II) particle swarm optimization (PSO), (III) genetic algorithm (GA). In JTPP-GD, a  $\Delta E_{\text{CO}}$  predictor network was jointly trained with the encoder and decoder. This network directly predicted the optimal  $\Delta E_{\text{CO}}$  based on latent vector encoded from surface structure, without information about adsorbed CO molecules and adsorption sites. The  $\Delta E_{\text{CO}}$  of generated surfaces were then optimized using gradient descent. As shown in Fig. 3a, property optimization based on the BSA algorithm demonstrates the best efficiency compared to the JTPP-GD, PSO, and GA approaches. Notably, the jointly trained latent space vectors– $\Delta E_{\text{CO}}$  predictor constantly failed to optimize, with the proportion of surfaces generated in each generation with  $|\Delta E_{\text{CO}} + 0.67| \leq 0.15$  eV remaining around 20% due to its inaccuracy (MAE = 0.402 eV on testing data).

Moreover, as shown in Fig. 3b, a distinctive feature of the BSA optimization process is the approximately 55% similarity between the surfaces generated in successive BSA steps. This continuous generation of novel and superior surfaces, even after identifying those with the lowest  $|\Delta E_{\text{CO}} + 0.67|$ , demonstrates MAGECS's capability to transcend local minima and undertake a global exploration of the chemical space. More importantly, among the generated surfaces, we found a number of them have been experimentally verified to exhibit high CO<sub>2</sub>RR performance in previous studies (Fig. 3b)<sup>3,35–42</sup>. As shown in Figure S7, these rediscovered surfaces indeed have low  $|\Delta E_{\text{CO}} + 0.67|$ , demonstrating the reliability of MAGECS in generating highly active surface structures for CO<sub>2</sub>RR.

While these generated structures exhibit commendable CO<sub>2</sub>RR activity, it is imperative to ensure their validity and diversity. We first applied the structure validity and diversity evaluation methods from the CDVAE work, showing that our CDVAE model trained on the GASpy database achieved comparable or superior COV-R (diversity) and COV-P (quality) compared to that trained on the Materials Project database (Table S1). However, the structure validity metric used by CDVAE only ensures that the distance between any two atoms is greater than 1 Å, which does not consider the thermodynamic stability of the structure.

Thus, we employed formation energy ( $E_f$ ) as the structure evaluation metric and utilized a high-precision graph neural network model (MEGNet) to predict  $E_f$ , bypassing the need for time-consuming DFT calculations. As shown in Figure S8a, the  $E_f$  of generated surfaces predicted by MEGNet have a mean value and distribution closely matching those of the training and validation surfaces. This indicates the capability of generating high-quality structures of the generation model in our inverse design framework. Furthermore, we validated our structure evaluation metric by adding random noise to atom coordinates within structures. As the noise level increases, the structural validity should deteriorate. This noise-distinguished method proved that MEGNet-predicted formation energy is an effective structure evaluation metric as it increases with noise, leveling off beyond 0.5, as seen in training and validation sets (details discussed in Supplementary Method S1).

After validating the rationality of 250,000 generated surfaces, an in-depth analyze of the elemental, compositional, and structural distributions across these surfaces helps identify key factors in CO<sub>2</sub>RR. We first visualized the frequency of occurrence for each element across the 250,000 alloy surfaces (Fig. 3c), where Cu and Al are emerged as the most prevalent elements. To further elucidate combinations of elements favorable for CO<sub>2</sub>RR, we computed the average of the smallest ten  $|\Delta E_{\text{CO}} + 0.67|$  values for binary alloys (Fig. 3d). Overall, binary alloys comprising Cu and Al in combination with other elements exhibit the most favorable CO<sub>2</sub>RR activity, alongside numerous high-activity binary alloy surfaces yet to be explored, such as AlPt, AlPd, and SnPd. Beyond binary alloys, 250,000 surfaces include pure metals, ternary and quaternary alloys, with 1,549 out of a total of 4573 compositions satisfying  $|\Delta E_{\text{CO}} + 0.67| \leq 0.15$  eV. Figure 3e showcases the foremost ten compositions, with AlCu, CuAu, AlPd, and AlPt topping the list, meanwhile highlighting promising yet unexplored compositions like CuAlSe (23<sup>rd</sup>) and SnPd (41<sup>st</sup>). These statistical analyses on elements and compositions offer significant guidance for designing CO<sub>2</sub>RR alloys and align with experimental evidence. Specifically, it is well-known that Cu is the most used element for CO<sub>2</sub>RR and various Cu-based alloys like CuAl, CuAu, CuPd, CuGa have demonstrated the exceptional ability in reducing CO<sub>2</sub> to diverse product<sup>3,36,43–47</sup>. CuAl alloy, in particular, has been experimentally demonstrated to have state-of-the-art Faraday efficiency in producing ethylene as well<sup>3</sup>.

Furthermore, we conducted a statistical analysis of the bulk symmetry of the generated surfaces. Since the surface structures were directly generated via the CDVAE model, we determined their bulk symmetry and surface orientation by a workflow that involved removing the vacuum layer, predicting the space group via XRD pattern<sup>48</sup>, and matching the cleaved surface from reconstructed bulk structures (see Supplementary Method 2 and Figure S14 for details). Following the identification of bulk symmetry, we found that close-packed arrangement with face-centered cubic (fcc) or hexagonal close-packed (hcp) phase constitutes the majority of the surfaces meeting the  $|\Delta E_{\text{CO}} + 0.67| \leq 0.15$  eV, accounting for 26.7% or 23.3%, respectively. Meanwhile, due to the presence of main group elements, some non-close-packed structures were also generated, including orthorhombic, tetragonal phases, etc. These results also support the reliability of our framework in generating stable structures.

### Identification of suitable surfaces for CO<sub>2</sub>RR via DFT calculations

Above our framework has successfully generated a large number of rational and potential surfaces with high CO<sub>2</sub>RR performance. Specifically, 89,875 surfaces satisfy  $|\Delta E_{\text{CO}} + 0.67| \leq 0.15$  eV (the first selection criterion). Next, considering the limitation of computational resources, we try to select the best few surfaces among these surfaces for DFT verification. During CO<sub>2</sub>RR, HER needs to be suppressed because it competes for active sites on surfaces with CO<sub>2</sub>RR. According to the

work by Greeley *et al.*<sup>49</sup>,  $\Delta G_{\text{H}}$  exhibits a volcano plot relationship with the experimental current density for HER, with  $\Delta G_{\text{H}} = 0.03$  eV ( $\Delta E_{\text{H}} = -0.27$  eV) being most favorable for HER. Thus, the  $|\Delta E_{\text{H}} + 0.27|$  should be as high as possible. On the other hand,  $\Delta E_{\text{H}}$  should not be too negative, otherwise the \*H intermediate will occupy too many active sites and cause catalyst poisoning. Thus, the second selection criterion is set as  $\Delta E_{\text{H}} + 0.27 \geq 0.6$  eV. In addition, the thermodynamic stability is also very important, which can be roughly evaluated by close to zero or negative formation energy  $E_f$ . Considering the computational error 0.1 eV/atom from DFT<sup>50</sup> and the MAE of 0.016 eV/atom in our trained ML model, we set  $E_f < -0.1$  eV/atom as the third criterion to make the generated surface as reasonable as possible.

The above three selection criteria for stable surfaces with high stability, activity and selectivity for CO<sub>2</sub>RR were achieved by accurate GNNs. The adsorption energies in the first two criteria were predicted by two DimeNet++ models. As depicted in Fig. 4a, b, the DimeNet++ models accurately predict CO and \*H adsorption energies on the independent test set with MAEs of 0.143 eV and 0.131 eV, and R<sup>2</sup> of 0.860 and 0.805, respectively. Considering the complexity of the training data (13,000 various structures), our models' accuracy is satisfactory and outperforms both the random forest model and GNN model in the literature<sup>8,51</sup> that used the same data set. The hyperparameters and training details of our DimeNet++ models are shown in Table S2 and Figure S15–16, respectively. As for the third selection criterion, the pre-trained MEGNet model for the formation energy achieves an MAE of 0.017 eV/atom on the independent test data after being trained with data from the OQMD dataset<sup>44</sup>. With the help of three GNNs, 110 best surfaces were selected based on the three selection criteria and are shown as dots in the rectangle area in Fig. 4c. Similar to the initial 250,000 surfaces, the most commonly used elements of 110 surfaces are still Cu and Al (Figure S17), and the most frequent element combinations are AlCu, AlCuSe and AlPd (Figure S18). Notably, after considering selectivity, the unexplored AlCuSe and the non-copper-based alloys SnPd, AlAu, and SbPt have emerged among the top 15 leading compositions.

Next, we carried out DFT verification on the selected 110 surfaces. First, all possible adsorption sites were enumerated on each surface, then DFT calculations were performed to determine the adsorption energies after adding \*CO and \*H species. The most negative adsorption energies across different sites on each surface were taken as the final adsorption energies. As shown in Fig. 4d, our DFT-calculated  $\Delta E_{\text{CO}}$  (a total of 1385 calculations on all sites) show good agreement with those predicted by the DimeNet++ model, with an MAE of 0.094 eV and R<sup>2</sup> of 0.813, even though differences may exist in calculation parameters between our calculations and previous literature<sup>8</sup>. More importantly, the subfigure of Fig. 4d shows that 97% of the 110 generated surfaces have a DFT-calculated  $|\Delta E_{\text{CO}} + 0.67| \leq 0.2$  eV for the most stable adsorption sites (with a maximum value of 0.210 eV), which is five times higher than that of the training data (19.6%), highlighting the effectiveness of MAGECS to inverse design alloy surfaces with potentially high CO<sub>2</sub>RR activity (small  $|\Delta E_{\text{CO}} + 0.67|$ ). As a result, the distribution of  $|\Delta E_{\text{CO}} + 0.67|$  of generated surfaces is much closer to 0 eV than that of surfaces in the database (Figure S19).

### Identification of suitable surfaces for CO<sub>2</sub>RR via experiments

However, due to the challenges in accurately modeling materials under catalytic conditions, a gap persists between DFT-calculated CO<sub>2</sub>RR performance and experimental values. Thus, we select promising alloys for experimental validation. Considering synthesizability, our selection was narrowed to alloys composed of three or fewer elements. The compositions frequently observed across the screened 110 surfaces are promising for superior CO<sub>2</sub>RR activity and selectivity. Thus, we first identified the most prevalent metal elements among 110 surfaces: Cu, Al, and Pd. Subsequently, we focused on surfaces primarily composed of Cu, Al, and Pd, selecting the top two compositions for

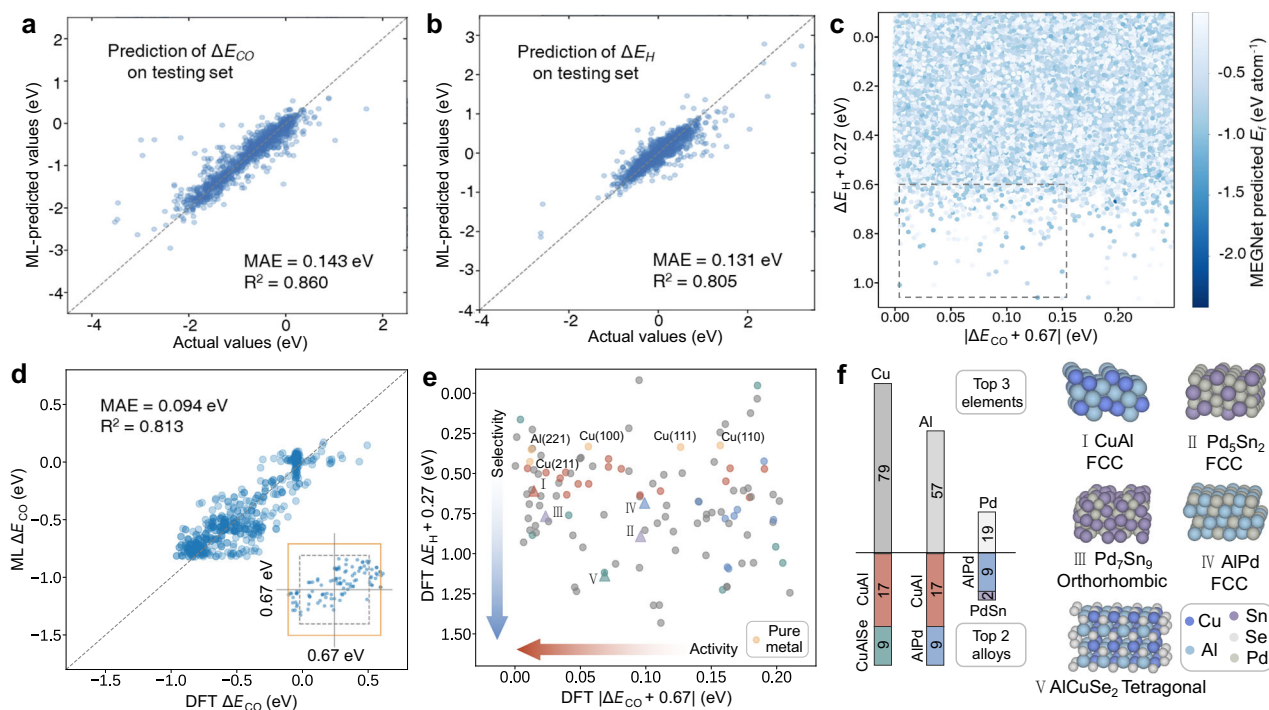


**Fig. 4 | DFT validation and screening of generated alloy surfaces for experimental validation.** DimeNet ++ predicted **a** CO and **b** H adsorption energies vs DFT calculated adsorption energies on independent testing data. **c**  $|\Delta E_{\text{CO}} + 0.67|$  vs  $|\Delta E_{\text{H}} + 0.27|$  of 250,000 surfaces, the color represents the value of MEGNet predicted formation energy. 110 surfaces selected for DFT validation are in the rectangle area. **d** DimeNet ++ predicted  $\Delta E_{\text{CO}}$  vs DFT calculated  $\Delta E_{\text{CO}}$  on 110 surfaces selected for DFT validation. The subfigure shows the range of ML-predicted and DFT-calculated  $\Delta E_{\text{CO}} + 0.67$  for the most stable adsorption sites of 110 surfaces, the

orange and grey rectangle border ranges from  $-0.2$  to  $0.2$  eV (orange solid line) and  $-0.15$  to  $0.15$  eV (grey dash line), respectively. **e** DFT calculated  $|\Delta E_{\text{CO}} + 0.67|$  vs  $|\Delta E_{\text{H}} + 0.27|$  of 110 surfaces. Pure metals, CuAl, AlPd, SnPd, CuAlSe and other surfaces are marked with orange, red, blue, purple, green and grey points, respectively. Five surfaces selected for experimental validation are in the rectangle area and marked with triangles. **f** Top 3 metal elements among 110 surfaces and top 2 alloys of Cu, Al, and Pd-based surfaces. Structure, crystal system of bulk and miller index of the five example surfaces.

each (Fig. 4e). As a result, CuAl, AlPd,  $\text{Sn}_2\text{Pd}_5$ ,  $\text{Sn}_9\text{Pd}_7$ , and CuAlSe<sub>2</sub> were chosen, with their example surface structures and bulk crystal systems illustrated in Fig. 4f.

However, experimentally synthesized surfaces typically exhibit a mix of crystal orientations (Miller indices), with the dominant ones corresponding to the strongest XRD peaks. Due to this complexity, studies on surface catalytic reactions often focus on modeling these dominant orientations, as they most accurately represent the catalyst behavior<sup>52–54</sup>. Therefore, to experimentally validate the CO<sub>2</sub>RR performance of predicted CuAl, AlPd,  $\text{Sn}_2\text{Pd}_5$ ,  $\text{Sn}_9\text{Pd}_7$ , and CuAlSe<sub>2</sub> surfaces, we aimed to synthesize these structures with bulk XRD pattern and surface orientation on XRD peak that match the generated surface structures. Successfully, the synthesized surfaces that match the generated structures (Figure S20) were situated close to the edge of the screening rectangle (Figure S21), which were theoretically predicted to exhibit high CO<sub>2</sub>RR activity and selectivity.

The Scanning electron microscopy (SEM) images (Figure S22) and transmission electron microscopy (TEM) images (Fig. 5a) show that CuAl alloys exist as amorphous nanoblocks. The high-resolution TEM (HRTEM) image of the CuAl (inset in Fig. 5a) displays clear lattice fringes with a lattice distance of  $0.2$  nm corresponding to the  $(-311)$  plane of the prepared catalyst, which aligns with the Miller index of the generated CuAl surface. The energy dispersive spectroscopy (EDS) elemental mapping analysis indicates a homogeneous distribution of the two elements in the alloys without significant phase separation (Fig. 5a). The powder X-ray diffraction (XRD) pattern (Fig. 5b) confirmed the successful synthesis of the alloy. The surface elemental composition of CuAl alloys was investigated through X-ray photoelectron spectroscopy (XPS) measurements, revealing the presence of Cu, Al, and O elements on the surface (Figure S23a). High-resolution Cu

LMM and Cu 2p spectra indicate the presence of metallic Cu and copper oxide (Figure S23b and c). Figure S23d illustrates the presence of metallic and oxidized aluminum states on the surface of the alloy. The presence of the atmosphere leads to partial oxidation of the surface of the synthesized nano-alloys. We evaluated the performance of CuAl in electrochemical CO<sub>2</sub>RR using the timed-current method in a flow-type cell equipped with a three-electrode system in a  $1$  M KOH solution. Gaseous and liquid products were analyzed using online gas chromatography and nuclear magnetic resonance (NMR) spectroscopy. The presented data demonstrate the high performance of CuAl catalysts in CO<sub>2</sub>RR reactions (Figs. 5c and 5g). At  $-0.7$  V vs. RHE, the catalyst exhibited the highest CO<sub>2</sub>RR performance, achieving an overall Faraday efficiency (FE) of  $87.73\%$  (Fig. 5c and S24). This significantly outperformed the pure Cu, whose FE of  $\text{C}_1 + \text{C}_2$  and  $\text{C}_2$  products was  $84.83\%$  and  $40.96\%$ , respectively, at  $-0.9$  V vs. RHE (Figure S25–26). Furthermore, the catalyst retained a relatively high overall FE after 24 hours of continuous electrolysis at  $-0.7$  V vs. RHE (Fig. 5h), presenting outstanding electrochemical stability. Notably, while the CuAl catalyst has been synthesized in previous studies<sup>3</sup>, the elemental ratio reported (Cu:Al =  $2:1$ ) differs from the  $1:1$  ratio in our catalyst.

In contrast, the  $\text{Pd}_5\text{Sn}_2$  materials synthesized through wet chemistry comprise agglomerated nanoparticles (Figure S27). TEM images also indicate that the alloy particles exhibit a uniform size of around  $10$  nm (Fig. 5d). HRTEM images showed the lattice spacings of  $0.22$  nm (inset in Fig. 5d), corresponding to the  $(111)$  planes of Pd and the Miller index of the generated  $\text{Pd}_5\text{Sn}_2$  surface. Additionally, EDS elemental mapping analysis demonstrates the uniform distribution of Pd and Sn across the chosen area (Fig. 5d). The XRD pattern illustrates that  $\text{Pd}_5\text{Sn}_2$  displays a pattern similar to that of Pd (JCPDS No. 46-1034), lacking peaks attributed to Sn-based compounds. However, a shift to



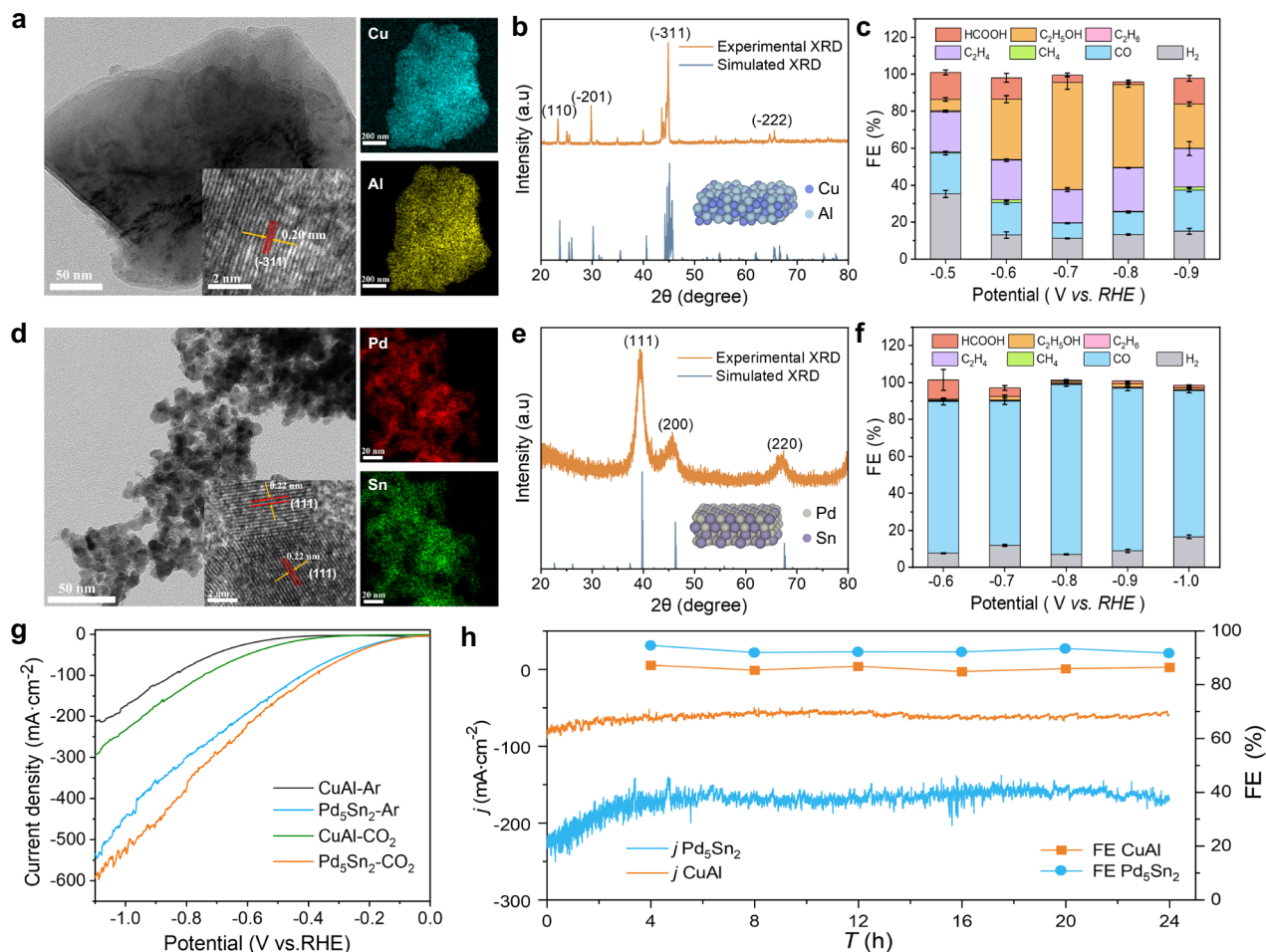


**Fig. 5 | Experimental validation of generated alloy surfaces.** **a** TEM images and EDS elemental mapping images of Cu, Al for CuAl alloys (inset: HRTEM image). **b** XRD patterns of CuAl alloys and simulated XRD of the bulk structure of generated CuAl surface (subfigure visualizes the generated CuAl surface). **c** The FEs towards CO<sub>2</sub>RR products under a range of applied potentials in 1 M KOH (pH = 13.93) of CuAl alloys. **(d)** TEM images and EDS elemental mapping images of Pd, Sn for Pd<sub>5</sub>Sn<sub>2</sub> alloys (inset: HRTEM image). **e** XRD patterns of Pd<sub>5</sub>Sn<sub>2</sub> alloys and

simulated XRD of the bulk structure of generated Pd<sub>5</sub>Sn<sub>2</sub> surface (subfigure visualizes the generated Pd<sub>5</sub>Sn<sub>2</sub> surface). **f** FEs towards CO<sub>2</sub>RR products under a range of applied potentials in 1 M KOH of Pd<sub>5</sub>Sn<sub>2</sub> alloys. **g** LSV curves of CuAl alloys and Pd<sub>5</sub>Sn<sub>2</sub> alloys (scan rate = 5 mV s<sup>-1</sup>, catalyst mass loading = 1 mg cm<sup>-3</sup>). **h** Electrochemical stability test of the CuAl catalyst at -0.7 V vs. RHE and Pd<sub>5</sub>Sn<sub>2</sub> catalyst at -0.8 V vs. RHE at room temperature (FE is the total of the CO<sub>2</sub>RR to carbon products, gas flow = 20 sccm).

lower angles, in comparison to the pattern of Pd, suggests the uninformed doping of Sn into Pd (Fig. 5e). The survey XPS spectrum in (Figure S28) validates the presence of Pd and Sn elements on the nanoparticle surface. The assessment of Pd<sub>5</sub>Sn<sub>2</sub> in CO<sub>2</sub>RR was conducted under identical conditions. The catalyst achieved a faradaic efficiency exceeding 80% for the conversion of CO<sub>2</sub> to carbon products within the voltage range of -0.6 to -1.0 V vs RHE. Moreover, the faradaic efficiency (FE) for CO production remained steady at approximately 80% across the potential window, consistently generating CO with an average FE as high as 91.86% at -0.8 V vs RHE (Fig. 5f and S29). By comparison, the pure Pd and Sn only achieve FE of 50.09% at -0.6 V vs. RHE and 76.63% at -0.9 V vs. RHE, respectively, considerably lower than that of Pd<sub>5</sub>Sn<sub>2</sub> (Figure S30-33). Furthermore, Pd<sub>5</sub>Sn<sub>2</sub> maintained good stability in terms of FE of ~90% for CO<sub>2</sub>RR to carbon products at -0.8 V vs. RHE, remaining stable for 24 hours. In addition, Pd<sub>5</sub>Sn<sub>9</sub>, PdAl, and CuAlSe<sub>2</sub> were synthesized and all exhibited good CO<sub>2</sub>RR properties. The FEs for CO<sub>2</sub>RR to carbon products at specific voltages were all above 70% (Figure S34-44).

## Discussion

In summary, we have developed a general property-to-structure inverse design framework, MAGECS, which enables comprehensive exploration of vast chemical spaces and consistent generation of high-

quality material structures with target properties. This merit has been realized by innovatively integrating the bird swarm algorithm with state-of-the-art GNNs to effectively navigate the generative model toward materials with superior properties. The efficiency of MAGECS has been robustly demonstrated in the application of designing alloy surfaces for electrocatalytic CO<sub>2</sub>RR. A total of 250,000 rational and promising alloy surfaces were generated and 110 surfaces were subjected to first-principles calculations, due to their high predictive activity, selectivity, and stability. Significantly, the ratio of surfaces exhibiting high activity for CO<sub>2</sub>RR surpasses the training data benchmarks by a remarkable 2.5 times. On this basis, we synthesized and characterized five predicted alloys—CuAl, AlPd, Sn<sub>2</sub>Pd<sub>5</sub>, Sn<sub>9</sub>Pd<sub>7</sub>, and CuAlSe<sub>2</sub>. Among these, two alloys demonstrated approximately 90% Faradaic efficiency in CO<sub>2</sub>RR (high selectivity) and -600.6 mA/cm<sup>2</sup> and -296.2 mA/cm<sup>2</sup> current density under -1.1 V vs. RHE (high activity), with CuAl notably achieving 76% efficiency for C<sub>2</sub> products.

While our developed MAGECS demonstrates considerable capability in the inverse design of CO<sub>2</sub>RR electrocatalysts, there is still potential for further enhancements. Specifically, the accuracy of supervised GNN models presents room for improvement, as it currently limits the efficiency of our framework. Moreover, numerous functional materials, such as photocatalysts, require the simultaneous

satisfaction of multiple target properties including band gap, band edge, and stability. This necessitates the development of efficient multi-objective optimization strategies integrated with inverse design. Finally, considering the gap between thermodynamic stability and experimental synthesizability, integrating a universal model to predict synthesizability into our framework will undoubtedly catapult MAGECS to a greater height.

## Methods

### Crystal diffusion variational autoencoder

CDVAE consists of two GNNs (GemNet and DimeNet++) are used in this work) and three fully connected neural networks (NNs). While training, the DimeNet++ was trained to encode the original material structures into latent vectors and the GemNet was trained to denoise the noised material structures. The main hyperparameters for training CDVAE are shown in Table S4-6. All main loss functions on the training set and validation set converge well (Figure S46), demonstrating the training of CDVAE was adequate.

### Supervised GNN

Six popular supervised GNNs (CGCNN<sup>55</sup>, SchNet<sup>56</sup>, DimeNet++<sup>33,34</sup>, PaiNN<sup>57</sup>, GemNet<sup>58</sup> and GemNet-OC<sup>51</sup>) were tested for surface property prediction. As shown in Figure S47, the CGCNN and SchNet, which did not consider the information of interatomic angles, showed a clear performance gap with other GNNs on testing data. The DimeNet++ had comparable performance to PaiNN and outperformed the GemNet and GemNet-OC on testing data. Moreover, the DimeNet++ exhibited faster training speed than PaiNN (1.2x), GemNet (2x) and GemNet-OC (2.5x). Thus, the DimeNet++ was utilized to predict CO and H adsorption energies in this work. The main hyperparameters of training these GNNs are listed in Table S2, 7–11.

### Bird swarm algorithm

The BSA algorithm was inspired by the swarm intelligence observed in bird swarms. Birds exhibit three main behaviors: foraging, vigilance, and flight. These social interactions help birds find food and avoid predators, increasing their chances of survival. BSA models these behaviors with five simplified rules (see Supplementary methods S3 and Figure S2), endowing it with good optimization efficiency and the ability to escape local optima. Thus, the BSA is used for global exploration of the chemical space in our framework. Table S3 shows the hyperparameters of performing BSA. We wrote the BSA with python language and the code is available in <https://github.com/szl666/CO2RR-inverse-design>.

### Automated DFT calculations

All the DFT energies in this work were calculated by the VASP package<sup>59</sup>. The slabs with all kinds of adsorbates were automatically built using the Pymatgen package<sup>60</sup>. The structure optimization was performed using a plane wave-based group with a 350 eV cutoff energy and the RPBE exchange-correlation function. The energy and force convergence criterion are set to be  $5 \times 10^{-4}$  eV and  $0.02 \text{ eV} \cdot \text{\AA}^{-1}$ , respectively. The Gibbs free energy difference  $\Delta G$  of the adsorbates before and after adsorption on the surface was calculated to consider temperature's influence. The standard hydrogen electrode approximation was used to bypass electron energy calculation. The free energy was calculated by Eq. (1):

$$G = E + ZPE - TS \quad (1)$$

where  $E$  is energy,  $ZPE$  and  $S$  are the zero-vibration energy and entropy, respectively, which can be obtained by VASP vibrational calculation.  $T$  is the temperature setting to 300 K.

### Material synthesis

All chemicals are of analytical grade and used without further purification. Copper powder, aluminum powder and palladium powder were purchased from Hebei Jiuyue New Material Technology Co. Palladium diacetylacetonate and selenium powder were bought from Aladdin.  $\text{SnCl}_2$ ,  $\text{NaBH}_4$ , Polyvinyl pyrrolidone (PVP) and ethylene glycol were bought from Mackli. Ethanol, potassium format,  $\text{N}_2\text{H}_4 \cdot \text{H}_2\text{O}$  and KOH were purchased from Sinopharm. The ion exchange membrane was purchased from Dupont. Carbon paper (CP) was purchased from Avcarb. The detail of the synthesis of CuAl, CuAlSe<sub>2</sub>, PdAl, Pd<sub>15</sub>Sn<sub>6</sub> and Pd<sub>15</sub>Sn<sub>6</sub> are discussed in Supplemental Methods S4. The EDS results of above-mentioned materials are shown in Table S12.

### Material characterization

The phase and crystallinity of samples were characterized by X-ray diffraction (Miniflex6000, Rigaku) at 40 kV and 15 mA using Cu-K $\alpha$  radiation ( $\lambda = 1.54178 \text{ \AA}$ ) at room temperature and scan speed was  $15^\circ/\text{min}$ . Morphology of the catalysts was characterized by High resolution field emission scanning electron microscope (FEI Inspect F50) and Thermo Scientific Talos F200X transmission electron microscope (STEM, Talos F200X). X-ray photoelectron spectroscopy (XPS) was performed on Escalab 250Xi. NMR spectra were recorded on a AVANCE III HD 600 MHz. In which 500  $\mu\text{L}$  electrolyte was added with 100  $\mu\text{L}$  D<sub>2</sub>O and dimethyl sulfoxide (DMSO) was added as the internal standard.

### Electrochemical characterization

The electrocatalytic performance of a three-electrode system for CO<sub>2</sub>RR was investigated on a CHI 760E electrochemical workstation at room temperature. The flow cell (Figure S43) assembly used consists of a gas flow chamber, a cation chamber and an anion chamber ( $0.5 \times 0.5 \times 0.5 \text{ cm}^3$ ). Each chamber has an inlet and outlet for electrolytes or gas. A commercial platinum sheet ( $0.5 \times 0.5 \text{ cm}^2$ ) is used as anode and an Ag|AgCl is acted as the reference<sup>1</sup>. M KOH (pH =  $13.93 \pm 0.028$ ) are used as the cathode and anode electrolyte, respectively. The fabrication process for the working electrode involved adding 100  $\mu\text{L}$  of catalyst ink dropwise to the carbon paper ( $0.5 \times 0.5 \text{ cm}^2$ ) electrode to achieve a loading of approximately  $1 \text{ mg cm}^{-2}$ . The electrode was then dried under an infrared lamp. The cathode chamber and anode chamber were separated by a piece of ion exchange membrane. Electrolytes were cycled at  $20 \text{ mL min}^{-1}$  and the CO<sub>2</sub> gas was supplied at rate of  $20 \text{ sccm}$ .

All potentials in our experiments are converted to reversible hydrogen electrode (RHE) reference scale by using the Nernst function as below,

$$E (\text{vs. RHE}) = E (\text{vs. Ag|AgCl}) + 0.197 \text{ V} + 0.059 \times \text{pH}$$

The detail about the products analysis is discussed in Supplementary Methods S5 and Figure S44-45.

### Data availability

The DFT calculated  $|\Delta E_{\text{CO}} + 0.67|$  and  $\Delta E_{\text{H}}$  of the 110 generated surfaces after screening are provided in Supplementary Data 1 and Source Data files. Source data are provided with this paper. Source Data file has been deposited in Figshare under [https://figshare.com/articles/dataset/Generated\\_surfaces/27986531](https://figshare.com/articles/dataset/Generated_surfaces/27986531)<sup>61</sup>. Source data are provided with this paper.

### Code availability

The codes to perform the inverse design of novel CO<sub>2</sub>RR electrocatalysts using MAGECS along with the result analysis and visualization are available at <https://github.com/szl666/CO2RR-inverse-design><sup>62</sup>.



## References

- Butler, K. T., Davies, D. W., Cartwright, H., Isayev, O. & Walsh, A. Machine learning for molecular and materials science. *Nature* **559**, 547–555 (2018).
- Huang, B. & von Lilienfeld, O. A. Ab Initio Machine Learning in Chemical Compound Space. *Chem. Rev.* **121**, 10001–10036 (2021).
- Zhong, M. et al. Accelerated discovery of CO<sub>2</sub> electrocatalysts using active machine learning. *Nature* **581**, 178–183 (2020).
- Han, Z. et al. Machine-learning-assisted design of a binary descriptor to decipher electronic and structural effects on sulfur reduction kinetics. *Nat. Catal.* **6**, 1073–1086 (2023).
- Esterhuizen, J. A., Goldsmith, B. R. & Linic, S. Interpretable machine learning for knowledge generation in heterogeneous catalysis. *Nat. Catal.* **5**, 175–184 (2022).
- Lu, S., Zhou, Q., Guo, Y. & Wang, J. On-the-fly interpretable machine learning for rapid discovery of two-dimensional ferromagnets with high Curie temperature. *Chem* **8**, 769–783 (2022).
- Song, Z. et al. Distilling universal activity descriptors for perovskite catalysts from multiple data sources via multi-task symbolic regression. *Mater. Horiz.* **10**, 1651–1660 (2023).
- Tran, K. & Ulissi, Z. W. Active learning across intermetallics to guide discovery of electrocatalysts for CO<sub>2</sub> reduction and H<sub>2</sub> evolution. *Nat. Catal.* **1**, 696–703 (2018).
- Weng, B. et al. Simple descriptor derived from symbolic regression accelerating the discovery of new perovskite catalysts. *Nat. Commun.* **11**, 3513 (2020).
- Oganov, A. R., Lyakhov, A. O. & Valle, M. How evolutionary crystal structure prediction works-and why. *Acc. Chem. Res.* **44**, 227–237 (2011).
- Sanchez-Lengeling, B. & Aspuru-Guzik, A. Inverse molecular design using machine learning: Generative models for matter engineering. *Science* **361**, 360–365 (2018).
- Noh, J., Gu, G. H., Kim, S. & Jung, Y. Machine-enabled inverse design of inorganic solid materials: promises and challenges. *Chem. Sci.* **11**, 4871–4881 (2020).
- Lu, S., Zhou, Q., Chen, X., Song, Z. & Wang, J. Inverse design with deep generative models: next step in materials discovery. *Natl. Sci. Rev.* **9**, 9–11 (2022).
- Noh, J. et al. Inverse Design of Solid-State Materials via a Continuous Representation. *Matter* **1**, 1370–1384 (2019).
- Long, T. et al. Constrained crystals deep convolutional generative adversarial network for the inverse design of crystal structures. *npj Comput. Mater.* **7**, 66 (2021).
- Kim, S., Noh, J., Gu, G. H., Aspuru-Guzik, A. & Jung, Y. Generative Adversarial Networks for Crystal Structure Prediction. *ACS Cent. Sci.* **6**, 1412–1420 (2020).
- Kim, B., Lee, S. & Kim, J. Inverse design of porous materials using artificial neural networks. *Sci. Adv.* **6**, eaax9324 (2020).
- Zhao, Y. et al. High-Throughput Discovery of Novel Cubic Crystal Materials Using Deep Generative Neural Networks. *Adv. Sci.* **8**, 14–16 (2021).
- Siriwardane, E. M. D., Zhao, Y., Perera, I. & Hu, J. Generative design of stable semiconductor materials using deep learning and density functional theory. *npj Comput. Mater.* **8**, 164 (2022).
- Yao, Z. et al. Inverse design of nanoporous crystalline reticular materials with deep generative models. *Nat. Mach. Intell.* **3**, 76–86 (2021).
- Xie, T., Fu, X., Ganea, O.-E., Barzilay, R. & Jaakkola, T. Crystal Diffusion Variational Autoencoder for Periodic Material Generation. In *10th International Conference on Learning Representations (ICLR, 2022)*.
- Lu, S. et al. Accelerated discovery of stable lead-free hybrid organic-inorganic perovskites via machine learning. *Nat. Commun.* **9**, 3405 (2018).
- Choudhary, K. et al. The joint automated repository for various integrated simulations (JARVIS) for data-driven materials design. *npj Comput. Mater.* **6**, 173 (2020).
- Ward, L. et al. Matminer: An open source toolkit for materials data mining. *Comput. Mater. Sci.* **152**, 60–69 (2018).
- De Breuck, P.-P., Hautier, G. & Rignanese, G.-M. Materials property prediction for limited datasets enabled by feature selection and joint learning with MODNet. *npj Comput. Mater.* **7**, 83 (2021).
- Yang, H., Chen, T. & Huang, N. An adaptive bird swarm algorithm with irregular random flight and its application. *J. Comput. Sci.* **35**, 57–65 (2019).
- Meng, X.-B., Gao, X. Z., Lu, L., Liu, Y. & Zhang, H. A new bio-inspired optimisation algorithm: Bird Swarm Algorithm. *J. Exp. Theor. Artif. Intell.* **28**, 673–687 (2016).
- Artz, J. et al. Sustainable Conversion of Carbon Dioxide: An Integrated Review of Catalysis and Life Cycle Assessment. *Chem. Rev.* **118**, 434–504 (2018).
- Klankermayer, J., Wesselbaum, S., Beydoun, K. & Leitner, W. Selective Catalytic Synthesis Using the Combination of Carbon Dioxide and Hydrogen: Catalytic Chess at the Interface of Energy and Chemistry. *Angew. Chem. Int. Ed.* **55**, 7296–7343 (2016).
- Arakawa, H. et al. Catalysis research of relevance to carbon management: progress, challenges, and opportunities. *Chem. Rev.* **101**, 953–996 (2001).
- Yu, L. et al. Double-Atom Catalysts Featuring Inverse Sandwich Structure for CO<sub>2</sub> Reduction Reaction: A Synergetic First-Principles and Machine Learning Investigation. *ACS Catal.* **13**, 9616–9628 (2023).
- Liu, X. et al. Understanding trends in electrochemical carbon dioxide reduction rates. *Nat. Commun.* **8**, 15438 (2017).
- Gasteiger, J., Giri, S., Margraf, J. T. & Günnemann, S. Fast and Uncertainty-Aware Directional Message Passing for Non-Equilibrium Molecules. In *Machine Learning for Molecules Workshop (NeurIPS, 2020)*.
- Gasteiger, J., Groß, J. & Günnemann, S. Directional Message Passing for Molecular Graphs. In *8th International Conference on Learning Representations (ICLR, 2020)*.
- Peng, L. et al. Self-growing Cu/Sn bimetallic electrocatalysts on nitrogen-doped porous carbon cloth with 3D-hierarchical honeycomb structure for highly active carbon dioxide reduction. *Appl. Catal. B Environ.* **264**, 118447 (2020).
- Ma, S. et al. Electroreduction of Carbon Dioxide to Hydrocarbons Using Bimetallic Cu–Pd Catalysts with Different Mixing Patterns. *J. Am. Chem. Soc.* **139**, 47–50 (2017).
- Wang, L. et al. Bimetallic effects on Zn–Cu electrocatalysts enhance activity and selectivity for the conversion of CO<sub>2</sub> to CO. *Chem. Catal.* **1**, 663–680 (2021).
- Bagchi, D. et al. Structure-Tailored Surface Oxide on Cu–Ga Intermetallics Enhances CO<sub>2</sub> Reduction Selectivity to Methanol at Ultralow Potential. *Adv. Mater.* **34**, 2109426 (2022).
- Torelli, D. A. et al. Nickel–Gallium-Catalyzed Electrochemical Reduction of CO<sub>2</sub> to Highly Reduced Products at Low Overpotentials. *ACS Catal.* **6**, 2100–2104 (2016).
- Deng, Y. et al. On the Role of Sulfur for the Selective Electrochemical Reduction of CO<sub>2</sub> to Formate on CuS<sub>x</sub> Catalysts. *ACS Appl. Mater. Interfaces* **10**, 28572–28581 (2018).
- Zhang, X. et al. Atomic nickel cluster decorated defect-rich copper for enhanced C<sub>2</sub> product selectivity in electrocatalytic CO<sub>2</sub> reduction. *Appl. Catal. B Environ.* **291**, 120030 (2021).
- Beheshti, M., Kakooei, S., Ismail, M. C. & Shahrestani, S. Investigation of CO<sub>2</sub> electrochemical reduction to syngas on Zn/Ni-based electrocatalysts using the cyclic voltammetry method. *Electrochim. Acta* **341**, 135976 (2020).

43. Wang, C. et al. Mechanistic study of Cu-Ni bimetallic catalysts supported by graphene derivatives for hydrogenation of CO<sub>2</sub> to methanol. *J. CO<sub>2</sub> Util.* **49**, 101542 (2021).
44. Chen, X. et al. Controlling Speciation during CO<sub>2</sub> Reduction on Cu-Alloy Electrodes. *ACS Catal.* **10**, 672–682 (2020).
45. Vasileff, A. et al. Selectivity Control for Electrochemical CO<sub>2</sub> Reduction by Charge Redistribution on the Surface of Copper Alloys. *ACS Catal.* **9**, 9411–9417 (2019).
46. Feng, Y. et al. Laser-Prepared CuZn Alloy Catalyst for Selective Electrochemical Reduction of CO<sub>2</sub> to Ethylene. *Langmuir* **34**, 13544–13549 (2018).
47. Gu, Z. et al. Nanostructured Copper-Based Electrocatalysts for CO<sub>2</sub> Reduction. *Small Methods* **2**, 1800121 (2018).
48. Lee, B. & Do et al. Powder X-Ray Diffraction Pattern Is All You Need for Machine-Learning-Based Symmetry Identification and Property Prediction. *Adv. Intell. Syst.* **4**, 2200042 (2022).
49. Greeley, J., Jaramillo, T. F., Bonde, J., Chorkendorff, I. & Nørskov, J. K. Computational high-throughput screening of electrocatalytic materials for hydrogen evolution. *Nat. Mater.* **5**, 909–913 (2006).
50. Stevanović, V., Lany, S., Zhang, X. & Zunger, A. Correcting density functional theory for accurate predictions of compound enthalpies of formation: Fitted elemental-phase reference energies. *Phys. Rev. B* **85**, 115104 (2012).
51. Chanussot, L. et al. Open Catalyst 2020 (OC20) Dataset and Community Challenges. *ACS Catal.* **11**, 6059–6072 (2021).
52. Peng, C. et al. (111) Facet-oriented Cu<sub>2</sub>Mg Intermetallic Compound with Cu<sub>3</sub>-Mg Sites for CO<sub>2</sub> Electroreduction to Ethanol with Industrial Current Density. *Angew. Chem. Int. Ed.* **63**, e202316907 (2024).
53. Zhang, P., Yang, G., Li, F., Shi, J. & Zhong, H. Direct in situ photolithography of perovskite quantum dots based on photocatalysis of lead bromide complexes. *Nat. Commun.* **13**, 6713 (2022).
54. Fan, L. et al. High Entropy Alloy Electrocatalytic Electrode toward Alkaline Glycerol Valorization Coupling with Acidic Hydrogen Production. *J. Am. Chem. Soc.* **144**, 7224–7235 (2022).
55. Xie, T. & Grossman, J. C. Crystal Graph Convolutional Neural Networks for an Accurate and Interpretable Prediction of Material Properties. *Phys. Rev. Lett.* **120**, 145301 (2018).
56. Schütt, K. T., Sauceda, H. E., Kindermans, P.-J., Tkatchenko, A. & Müller, K.-R. SchNet – A deep learning architecture for molecules and materials. *J. Chem. Phys.* **148**, 241722 (2018).
57. Schütt, K. T., Unke, O. T. & Gastegger, M. Equivariant message passing for the prediction of tensorial properties and molecular spectra. In *Proceedings of the 38th International Conference on Machine Learning (ICML, 2021)*.
58. Gasteiger, J., Becker, F. & Günnemann, S. GemNet: Universal Directional Graph Neural Networks for Molecules. In *35th Conference on Neural Information Processing Systems* vol. 9 6790–6802 (NeurIPS, 2021).
59. Kresse, G. & Furthmüller, J. Efficient iterative schemes for ab initio total-energy calculations using a plane-wave basis set. *Phys. Rev. B* **54**, 11169–11186 (1996).
60. Ong, S. P. et al. Python Materials Genomics (pymatgen): A robust, open-source python library for materials analysis. *Comput. Mater. Sci.* **68**, 314–319 (2013).
61. Song Z. Generated surfaces, Figshare, <https://doi.org/10.6084/m9.figshare.27986531.v1> (2024).
62. Song Z. Inverse Design of Promising Electrocatalysts for CO<sub>2</sub> Reduction via Generative Models and Bird Swarm Algorithm, szl666/CO2RR-inverse-design: v0.1, <https://doi.org/10.5281/zenodo.14207637> (2024).

## Acknowledgements

This work was supported by the National Key Research and Development Program of China (grant 2022YFA1503103, 2021YFA1500700), the Natural Science Foundation of China (grant 22033002, 92261112, 22373013, T2321002), the Basic Research Program of Jiangsu Province (BK20232012, BK20222007) and Jiangsu Provincial Scientific Research Center of Applied Mathematics (BK20233002). We thank the National Supercomputing Center of Tianjin and the Big Data Computing Center of Southeast University for providing the facility support on the calculations.

## Author contributions

Z.S. and L.F. contribute equally to this work. Z.S., Q.Z., and J.W. conceived this work. Z.S. proposed the inverse design framework and wrote the code with guidance from J.W., Q.Z., and S.L.. Z.S. performed DFT calculations with guidance from C.L., Q.Z. and J.W., L.F. performed experimental validation and characterization. Z.S., L.F., S.L., Q.Z., C.L. and J.W. analyzed the data and co-wrote the manuscript, with input from the other authors.

## Competing interests

The authors declare no competing interest.

## Additional information

**Supplementary information** The online version contains supplementary material available at <https://doi.org/10.1038/s41467-024-55613-z>.

**Correspondence** and requests for materials should be addressed to Qionghua Zhou or Jinlan Wang.

**Peer review information** *Nature Communications* thanks the anonymous reviewers for their contribution to the peer review of this work. A peer review file is available.

**Reprints and permissions information** is available at <http://www.nature.com/reprints>

**Publisher's note** Springer Nature remains neutral with regard to jurisdictional claims in published maps and institutional affiliations.

**Open Access** This article is licensed under a Creative Commons Attribution-NonCommercial-NoDerivatives 4.0 International License, which permits any non-commercial use, sharing, distribution and reproduction in any medium or format, as long as you give appropriate credit to the original author(s) and the source, provide a link to the Creative Commons licence, and indicate if you modified the licensed material. You do not have permission under this licence to share adapted material derived from this article or parts of it. The images or other third party material in this article are included in the article's Creative Commons licence, unless indicated otherwise in a credit line to the material. If material is not included in the article's Creative Commons licence and your intended use is not permitted by statutory regulation or exceeds the permitted use, you will need to obtain permission directly from the copyright holder. To view a copy of this licence, visit <http://creativecommons.org/licenses/by-nc-nd/4.0/>.

© The Author(s) 2025